ACS OMEGA

http://pubs.acs.org/journal/acsodf

Article

N/O Co-doped Porous Carbons Derived from Coal Tar Pitch for Ultra-high Specific Capacitance Supercapacitors

Yuan-Jia Cao, Cui-Ying Lu,* Zhi-Wen Zhang, Zhen Wang, Yu-Hong Kang, Ting-Ting Yang, Guang-Hui Liu,* Xian-Yong Wei, and Hong-Cun Bai

Cite This: *ACS Omega* 2022, 7, 23342−23352

Read Online

ACCESS | Metrics & More | Article Recommendations | Supporting Information

ABSTRACT: In this paper, a series of N/O co-doped porous carbons (PCs) were designed and used to prepare coal tar pitch-based supercapacitors (SCs). The introduction of N/O species under the intervention of urea effectively improves the pseudocapacitance of PCs. The results show that the specific surface area of synthesized $N_3PC_{4\text{-}700}$ is 1914 m^2 g^{-1}, while the N and O contents are 1.3 and 7.2%, respectively. The unique interconnected pore structure and proper organic N/O co-doping, especially the introduction of pyridine-N and pyrrole-N, are beneficial for improving the electrochemical performance of PCs. In the three-electrode system, the specific capacitance and rate capability of $N_3PC_{4\text{-}700}$ are 532.5 F g^{-1} and 72.5% at the current densities of 0.5 and 20 A g^{-1}, respectively. In addition, the specific capacitance of $N_3PC_{4\text{-}700}$ in a coin-type symmetric device is 315.5 F g^{-1} at 0.5 A g^{-1}. The $N_3PC_{4\text{-}700}$ electrode provides an energy density of 43.8 W h kg^{-1} with a power density of 0.5 kW kg^{-1} and still maintains a value of 29.7 at 10 kW kg^{-1}. After 10,000 charge/discharge cycles, the retention rate was as high as 96.7%. In order to obtain high-performance carbon-based SCs, the effective identification and regulation of organic N/O species is necessary.

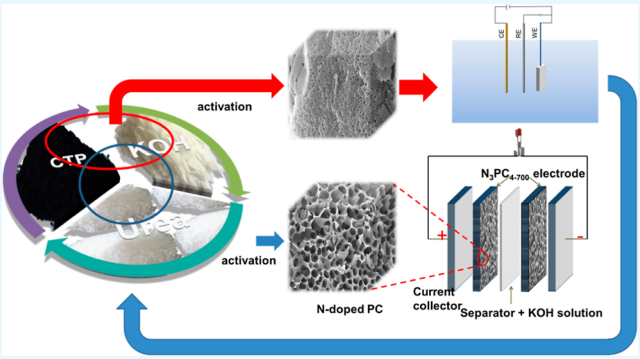

1. INTRODUCTION

Carbon-based supercapacitors (SCs) with high specific capacitance, good cycling stability, and high-rate capability are promising energy storage materials.[1] Porous carbon (PC) is one of the most commonly used electrode materials for SCs.[2] However, conventional ash-containing raw materials need to undergo multiple post-treatments before they can be made into PCs with good properties.[3] Coupled with the shortage of traditional fossil fuels and the rapid increase of greenhouse gases, the development of green, efficient, and low-cost carbon-based SCs has become a trend.[4]

Coal tar pitch (CTP) is a heavy fraction after distillation of coal tars, accounting for more than 55 wt %. This raw material has the advantages of high carbon content, low ash content, and good thermoplasticity, which are beneficial to the preparation of PCs.[5] Liu et al.[6] used the eutectic salt template strategy to prepare CTP-derived hierarchical PCs, which has a specific capacitance of 320 F g^{-1} at a current density of 0.1 A g^{-1}. Although CTP has been successfully used to synthesize PCs for SCs, due to the relatively low content of heteroatoms, the specific capacitance of electrode materials depends entirely on the behavior of electric double-layer capacitance, which makes the electrochemical performance of such conventional materials difficult to meet actual requirements.[7,8]

Heteroatom doping, especially N-doping, is one of the effective strategies to increase the specific capacitance of PCs.[9,10] The introduction of organic nitrogen species improves the hydrophilicity of the material surface and increases the electrical conductivity.[11] Obviously, the type and distribution of organic nitrogen species directly affect the performance of SCs. Pyrrole-N, pyridine-N, and graphite-N play different roles in enhancing electron-transfer activity,[12] providing electron pairs and pseudocapacitance,[13] and improving conductivity,[14] which are all conducive to realizing the effective electrochemical behavior. Zhong et al.[15] prepared CTP-derived N-doped PCs with melamine as the N-donor. The specific capacitance was 228 F g^{-1} at 1 A g^{-1}, and the capacitance retention was 94.2% after 1000 cycles. The relatively poor electrochemical performance may be related to the lower contents of pyrrole-N and pyridine-N. In contrast, the introduction of urea in the activation stage can not only provide sufficient pyridine-N, pyrrole-N, and oxynitrides but

Received: March 14, 2022
Accepted: June 9, 2022
Published: June 23, 2022

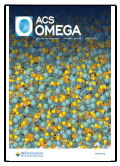

https://doi.org/10.1021/acsomega.2c01534
ACS Omega 2022, 7, 23342−23352

also further promote the synergistic pore-enlarging effect of KOH in the carbonization stage.[16] Therefore, the regulation of N-donors and N-doping behavior in the activation process is particularly important. In practical applications, the specific capacitance is not linearly proportional to specific surface area (SSA) but is closely related to the pore structure.[17] Charge storage, fast ion transport, and short ion diffusion require reasonably distributed pore structures (including micropores, mesopores, and macropores) to provide a relatively high SSA, low-resistance channels, and buffer reservoirs.[18,19] It can be seen that the regulation of surface active sites and pore size distribution is a breakthrough for obtaining electrode materials with high electrochemical performance.

As mentioned above, there are many related studies on CTP-based electrode materials for the preparation of supercapacitors.[15] However, related scholars have ignored the effect of different N-containing species on the electrochemical performance. In addition, there are few reports of a one-step preparation method that provides abundant oxynitrides and hierarchical pore structures. Noteworthily, the specific capacitance of CTP-based electrode materials is mostly limited to 300−400 F g^{-1}.[20] In view of this, CTP-derived N-doped PCs were directly prepared by one-pot carbonization using urea as the N-donor. The focus was on the distribution regulation of pyrrole-N and pyridine-N as well as the acquisition of hierarchical pore structures. In addition, the electrochemical performance of synthesized PCs and the related regulation mechanisms were also investigated.

2. EXPERIMENTAL SECTION

2.1. Materials. Low-temperature CTP (softening point 176 °C) was provided by Yulin Coal Chemical Industry Upgrade Technology R&D Center. CTP was pulverized to pass through a 200-mesh sieve (particle size ≤74 μm), followed by vacuum desiccation at 80 °C for 24 h before use. Polytetrafluoroethylene (PTFE) was purchased from Aladdin Chemical Co., Ltd., China. KOH (85 wt %) and HCl solution (37 wt %) were purchased from Shanghai Chemical Reagent Co., Ltd., China. Ethanol and urea are both analytically pure and purchased from Tianjin Kemiou Chemical Reagent Co., Ltd.

2.2. Synthesis of PCs. In a typical procedure, 3 g of CTP and a certain amount of KOH were ground and mixed uniformly. The mass ratio of KOH to CTP was X (X = 3, 4, or 5). The mixture was fed into a quartz tube and heated to the set temperature (Y = 600, 700, or 800 °C) at 3 °C min^{-1} under N_2 and kept for 3 h. After cooling to room temperature, the powder was placed in a 2 M HCl solution, stirred for 24 h, and washed repeatedly with deionized water to neutrality. Finally, the sample was vacuum-dried at 60 °C for 24 h before storing and named $PC_{X\text{-}Y}$.

Urea was added in the above grinding step, and the mass ratio of CTP to urea was Z (Z = 2, 3, or 4). The activation and post-treatment processes were consistent with the preparation of $PC_{X\text{-}Y}$. The resulting sample was named $N_ZPC_{X\text{-}Y}$.

2.3. Characterization. The pore structure of PCs was characterized by N_2 physisorption (Micromeritics ASAP 2460) at −196 °C. Brunauer−Emmett−Teller (BET) and density functional theory (DFT) methods were used to determine the SSA and pore size distribution, respectively. Scanning electron microscopy (SEM, ZEISS Sigma 300) was used to obtain the microstructure and surface morphology. The internal structure was determined by transmission electron microscopy (TEM, Talos F200X G2, superX). The X-ray diffraction (XRD) measurement was carried out with a Bruker Advance D8 XRD. A HORIBA Scientific Lab RAM HR Evolution laser confocal Raman spectrometer was used to record Raman spectra in the range of 4000−400 cm^{-1}. X-ray photoelectron spectroscopy (XPS) was performed on a Thermo Fisher Scientific Kα 1063 spectrophotometer. A JC2000C1 contact angle measuring instrument was used to explore the surface wettability of PCs.

2.4. Electrochemical Measurements. A PC, PTFE, and acetylene black were mixed at a mass ratio of 8:1:1 in 10 mL of ethanol and dried to obtain a working electrode slurry. A certain amount of mixed slurry was evenly coated on the pretreated Ni foam and vacuum-dried at 60 °C for 12 h. Before the test, the electrode material was soaked in a 6 M KOH solution for 12 h. Cyclic voltammetry (CV), galvanostatic charge−discharge (GCD), and electrochemical impedance spectroscopy (EIS) were performed on the CHI660E electrochemical workstation. In addition, the cyclic stability was tested on a LANDdt V7 test system (CT3002A).

In the three-electrode system, the Pt and Hg/HgO electrodes were used as the counter and reference electrodes, respectively. The CV and GCD tests were performed on the electrode sheet under the potential window of −1−0 V. The EIS measurements were carried out at an amplitude of 10 mV and a frequency of 10^{-2}−10^5 Hz.

The specific capacitance (C) of a single electrode was calculated by the following equation (eq 1)

$$C = \frac{I\Delta t}{m\Delta V} \tag{1}$$

where m (g) is the mass of the active material in the electrode, I (A) is the discharging current, and ΔV (V) is the potential change within the discharge time Δt (s).

The Coulombic efficiency (η) was calculated by using eq 2

$$\eta = \frac{t_d}{t_c} \tag{2}$$

where t_d (s) and t_c (s) are the discharge and charge times, respectively.

In the two-electrode system, a 6 M KOH solution was used as an electrolyte and two electrode sheets with the same mass were used as positive and negative electrodes to form a coin-shaped symmetrical device. The electrochemical tests were carried out on the electrochemical workstation and the LANDdt V7 test system. The specific capacitance of a single electrode was calculated from the GCD values according to the following equation (eq 3)

$$C = \frac{2I\Delta t}{m\Delta V} \tag{3}$$

where I (A) is the discharging current, m (g) is the average mass of the active material in the two electrodes, and ΔV (V) is the potential change within the discharge time Δt (s).

The energy density (E) and power density (P) were defined using eqs 4 and 5

$$E_t = \frac{C_t\Delta V^2}{2 \times 3.6} \tag{4}$$

$$P_t = \frac{3600E_t}{\Delta t} \tag{5}$$

where P_t (W kg^{-1}) is the specific power density, E_t (W h kg^{-1}) is the specific energy density, C_t (F g^{-1}) is the specific

https://doi.org/10.1021/acsomega.2c01534
ACS Omega 2022, 7, 23342−23352

capacitance, and ΔV (V) is the potential change within the discharge time Δt (s).

3. RESULTS AND DISCUSSION

3.1. Materials Characterization. As shown in Figure S1, all adsorption and desorption curves obey the Langmuir model. Obviously, micropores dominate the as-synthesized PCs, while the pore size is mostly concentrated within 2 nm. Such micropores provide a large number of attached electrolyte ion points. As further listed in Table 1, properly

Table 1. Textural Parameters of the Samples[a]

sample	SSA_{BET} ($m^2\ g^{-1}$)	SSA_{mic} ($m^2\ g^{-1}$)	PV ($m^3\ g^{-1}$) total	PV ($m^3\ g^{-1}$) micro	D_{ap} (nm)	specific capacitance ($F\ g^{-1}$)
PC_{4-600}	1960	1811	0.95	0.80	1.93	293.5
PC_{4-700}	2789	2628	1.35	1.18	1.93	309.7
PC_{4-800}	2258	2164	1.08	0.98	1.92	219.5
PC_{3-700}	1885	1822	0.84	0.77	1.78	295.5
PC_{5-700}	2569	2361	1.13	1.11	2.05	265.5
N_2PC_{4-700}	1222	1181	0.56	0.48	1.83	380.5
N_3PC_{4-700}	1914	1859	0.85	0.78	1.79	532.5
N_4PC_{4-700}	1286	1258	0.57	0.51	1.77	405.5

[a]D_{ap}: average pore size.

raising the temperature and increasing the ratio of KOH to CTP are beneficial to increase the SSA and pore volume (PV) of PCs. During the carbonization, KOH and dehydrated K_2O reacted with C and CO_2 produced by the rapid thermal condensation of CTP to release K and various reducing gases, such as CO and H_2, which are conducive to the formation of hierarchical pores.[21] As a result, PC_{4-700} exhibits the largest SSA and PV, while the proportion of micropore volume is 87.4%. These are the important factors for PC_{4-700} to provide a relatively large specific capacitance (309.7 F g^{-1} at 0.5 A g^{-1}).

As displayed in Figure 1a, N_ZPC_{4-700} exhibit type I/IV isotherms, indicating that micropores are also dominant in N-doped PCs. The clear hysteresis loops in the relative pressure range of 0.5−1 mean that there is still a small proportion of mesopores in PCs. Apparently, the organic nitrogen species formed by urea during the activation process played the role of ammoniation and pore expansion. As further demonstrated in Figure 1b, similar to PC_{4-700}, the pore size of N_ZPC_{4-700} is also mainly distributed in the range of 1−5 nm. Interestingly, the pore proportion of PC_{4-700} in the range of 1−3 nm is larger than that of N_ZPC_{4-700}, while the opposite is true around 4 nm. These results further confirmed that the introduction of urea enriched the pore type of PCs.

In contrast, the SSA and PV of PCs decreased significantly after N-doping (Table 1), which may be attributed to the partial conversion of micropores and mesopores to macropores under the effect of ammoniation.[22] It can also be clearly observed in Figure S2 that the pore size increases after N-doping, especially for N_3PC_{4-700}. In addition, proper introduction of N-containing species still maintains the higher SSA and PV of PCs. The hierarchical pore structure could increase ion diffusion channels, reduce diffusion resistance, and improve the utilization of micropores, which are beneficial to improve the electrochemical performance of PCs.[23,24] It can be seen that urea has the following advantages in the synthesis of N-doped PCs: (1) a higher N-doping efficiency, (2) better wettability, and (3) the evolution of abundant organic N-containing species, which are also related to the strong hydrogen bonds formed between O-containing species in CTP and urea.[25,26]

As shown in Figure 2a−c, N_ZPC_{4-700}, especially N_3PC_{4-700}, have a large number of uniformly distributed 3D pore structures, while the different pore sizes mean that the as-synthesized PCs have hierarchical pore characteristics. Compared with PC_{X-700}, the pore structure of N_3PC_{4-700} is more three-dimensional, with larger and more abundant pores (Figure S2). These changes are related to the synergistic activation of KOH and urea, making the porous network more regular and interconnected. TEM images (Figure 2d−f) further show that N_ZPC_{4-700} are composed of less carbon layers and have abundant edge defects. In addition, abundant interconnected channels and obviously rough surfaces are typical characteristics of amorphous PCs caused by high-temperature KOH activation. As further described in Figure 2g−i, the abundant non-graphitized micropores provide more active sites for the ion storage and transfer on electrode materials.

As shown in Figure 3a, all samples exhibited two typical diffraction peaks around 23° (002) and 43° (100). The relatively weak intensity of the (100) diffraction peak indicates

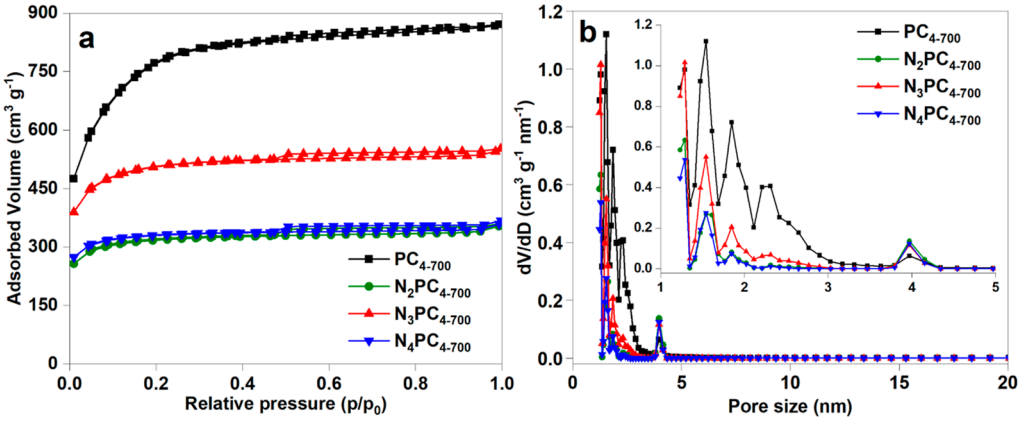

Figure 1. (a) N_2 adsorption/desorption isotherms and (b) pore size distribution curves of the samples.

https://doi.org/10.1021/acsomega.2c01534
ACS Omega 2022, 7, 23342−23352

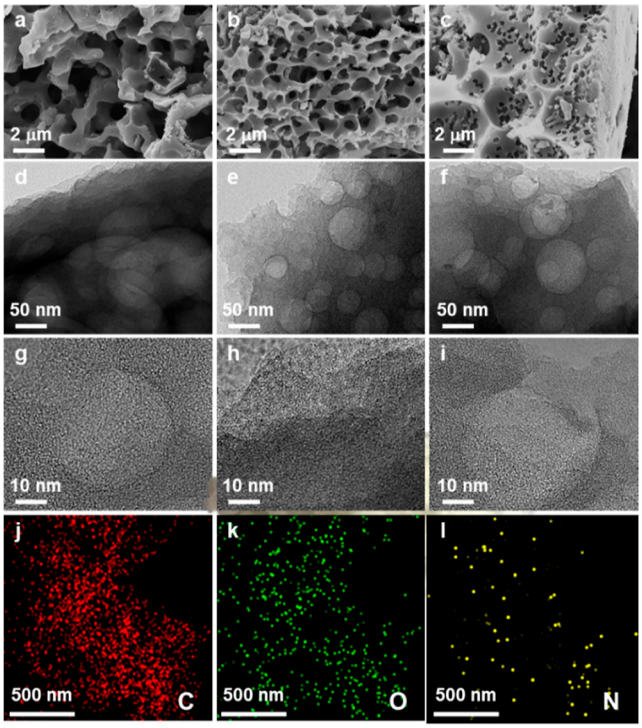

Figure 2. SEM images of (a) $N_2PC_{4\text{-}700}$, (b) $N_3PC_{4\text{-}700}$, and (c) $N_4PC_{4\text{-}700}$. TEM images of (d,g) $N_2PC_{4\text{-}700}$, (e,h) $N_3PC_{4\text{-}700}$, and (f,i) $N_4PC_{4\text{-}700}$. (j–l) Elemental mapping of $N_3PC_{4\text{-}700}$.

that PCs are dominated by amorphous carbon and structurally disordered.[27,28] The intensity difference of (002) diffraction peaks among PCs implies the correlation of the non-graphitized structure with urea content. All samples have higher diffraction peaks at low angles, indicating that there are a large number of micropores in PCs. The order of low-angle diffraction peak intensity is $N_3PC_{4\text{-}700}$ > $N_4PC_{4\text{-}700}$ > $N_2PC_{4\text{-}700}$, which is consistent with the BET analysis. As further exhibited in Figure 3b, peaks D and G represent the lattice defects of PCs and the in-plane stretching vibration of SP^2 hybrid C species, respectively.[29] The I_D/I_G is usually used to indicate the degree of lattice defects. The larger the ratio, the more lattice defects of PCs. The calculated I_D/I_G value of the sample is $N_3PC_{4\text{-}700}$ (1.01) > $N_4PC_{4\text{-}700}$ (0.98) > $N_2PC_{4\text{-}700}$ (0.94). It can be seen that when the carbon to nitrogen ratio is 3:1, the sample has the most defects, which is consistent with the XRD analysis.

As demonstrated in Figure S3 and Table S1, the N element was detected in all samples. As a N-donor, the introduction of urea effectively doped N species while significantly reducing the oxygen content in PCs. As shown in Figure 4a, the binding energies of pyridine-N (N_1), pyrrole-N (N_2), graphite-N (N_3), and N-oxides (N_4) are around 398, 400, 401, and 402.5 eV, respectively. The total proportion of N_1 and N_2 in all samples exceeds 55% (Table S2). Appropriate N-doping can effectively regulate the proportion of N_1–N_4 species. Obviously, the surface of $N_3PC_{4\text{-}700}$ has the highest proportion of N_1 and N_2 species. Figure 4b shows that the binding energies around 531, 532.5, and 534 eV in the O 1s spectrum of $N_3PC_{4\text{-}700}$ are attributed to > C═O, >C−O−, and −COOH functional groups, respectively.[30,31] As further listed in Table S2, the ratio of >C−O− is much higher than other O-containing moieties.

The introduction of organic N species, especially N_1 and N_2, is beneficial for increasing the wettability of electrode materials, adjusting the behavior of electron donors, and thereby improving the electrochemical performance.[32,33] As further summarized in Figure 5a, the water contact angle of $N_3PC_{4\text{-}700}$ was almost zero, implying that the introduction of N species greatly improves the hydrophilicity of PCs and increases the diffusion rate of electrolyte ions on the surface and inside of carbon materials. These differences are related to the unique distribution of nitrogen species in $N_3PC_{4\text{-}700}$.[12−14] In addition, the abundant oxygen-containing functional groups on its surface can also provide abundant reactive sites for additional pseudocapacitance (Figure 5b).[34] The change of chemical structure also proved the improvement of the hydrophilicity of $N_3PC_{4\text{-}700}$. Among them, the >C−O− part showing good electrochemical redox activity is retained in the high-temperature carbonization stage, which is more conducive to improving the pseudocapacitance of electrode materials.[35] As displayed in Figure S4 and Table S2, the binding energies around 289.1, 286.3, 285.0, and 284.1 eV in C 1s spectra are attributed to > C═O, >C−O−, >C−N<, and >C═C< moieties, respectively.[36] It can be seen that the total proportion of >C═O and >C−O− functional moieties in $N_3PC_{4\text{-}700}$ is moderate, while that of >C−N< functional groups is the highest, which further proves that $N_3PC_{4\text{-}700}$ has a suitable graphitized structure and is rich in defects and active edge sites.[37]

3.2. Electrochemical Characterization. *3.2.1. Three-Electrode System.* Figure 6 shows various electrochemical characterizations of $N_ZPC_{4\text{-}700}$ in the three-electrode system. The rectangular shape of the CV curve shows that $N_ZPC_{4\text{-}700}$

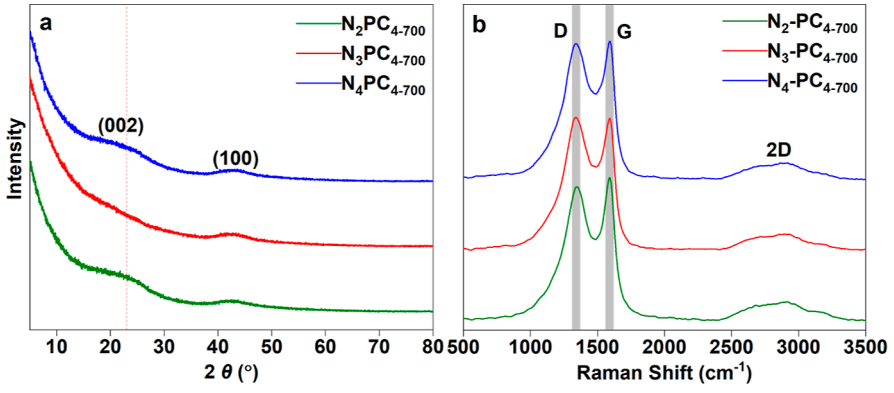

Figure 3. (a) XRD patterns and (b) Raman spectra of the samples.

https://doi.org/10.1021/acsomega.2c01534
ACS Omega 2022, 7, 23342−23352

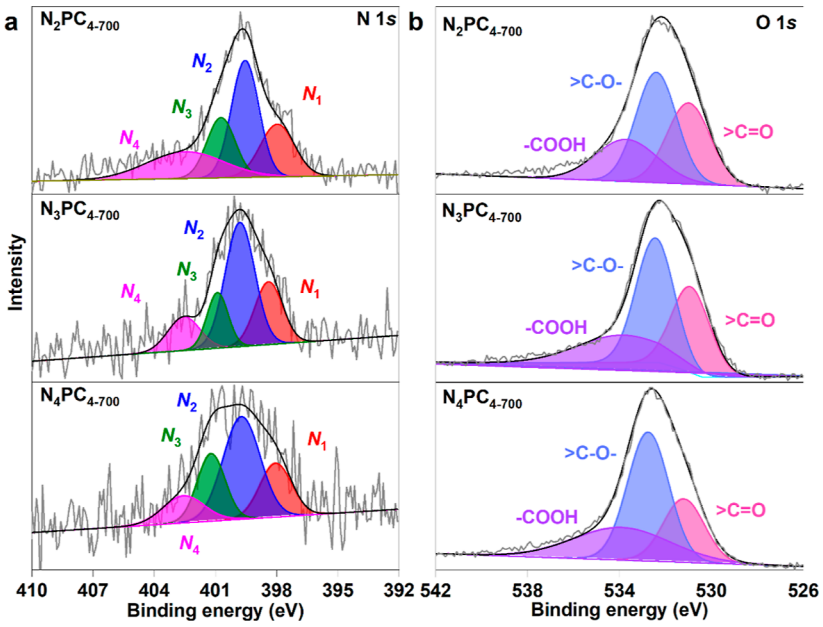

Figure 4. High resolution of samples (a) N 1s and (b) O 1s.

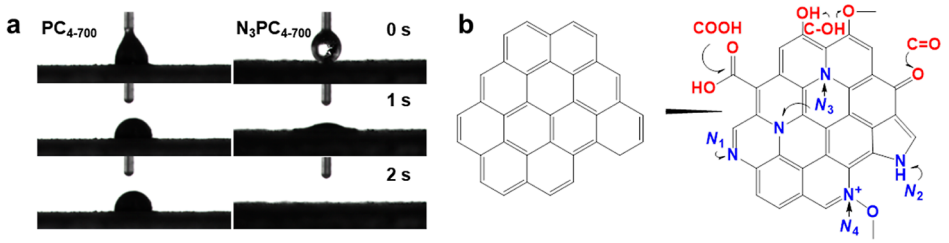

Figure 5. (a) Water contact angle tests of PC_{4-700} and N_3PC_{4-700} at different times and (b) schematic illustration for the possible chemical structure of N/O co-doped PCs.

have excellent double-layer capacitor behavior (Figure 6a). In addition, the redox process of −0.8−−0.3 V can be clearly observed on all CV curves, which should be attributed to the redox reaction of N/O functional groups.[38] The PC_{4-700} electrode has no obvious redox peak (Figure S5c), which proves that the pseudocapacitance of N_3PC_{4-700} mainly comes from the N species introduced by urea doping. In addition, N_3PC_{4-700} has the largest CV curve area (Figures 6a and S5a), indicating the highest specific capacitance. Figure 6b shows that the GCD curve shapes of N_ZPC_{4-700} electrodes are slightly deviated from the isosceles triangle, indicating that the energy storage of PCs is controlled by the electric double layer and pseudocapacitance behavior.[39,40] The GCD curves of the N_ZPC_{4-700} electrode have no obvious IR value, indicating that the internal resistance is relatively small. Furthermore, N_3PC_{4-700} has the longest discharge time and the largest specific capacitance, indicating that the urea dosage and activation temperature of N_3PC_{4-700} are the best conditions (Figures 6b and S5b).

The high specific capacitance of N_3PC_{4-700} is caused by the excellent pore structure and suitable doping amount of nitrogen species. On one hand, the reasonable hierarchical pore structure can provide more channels, which is beneficial to the efficient transport of electrolyte ions.[19] In addition, for the three nitrogen-doped PCs, N_3PC_{4-700} has the largest SSA_{mic} and micropore volume, implying the highest proportion of micropores, which in turn provides more attachment sites.[16] These physical structure changes are beneficial to improve the electrochemical performance of PCs.[41] On the other hand, rational doping of urea also introduces abundant N-containing groups, especially N_1 and N_2. For the physical structure, the increase of edge defects and surface wrinkle/distortion are beneficial to the improvement of electron transport efficiency. For the chemical structure, rational doping of nitrogen species enhances the wettability of PCs, which in turn facilitates the penetration and absorption of electrolyte ions.

As further shown in Figure S5d, the specific capacitance of N_3PC_{4-700} at 0.5 A g^{-1} is 532.5 F g^{-1}, which is much higher than that of PC_{4-700} (309.7 F g^{-1}). The significant increase in specific capacitance may be due to the following three reasons: (1) N_3PC_{4-700} has good hydrophilicity (Figure 5a), resulting in low diffusion resistance, which is beneficial to the storage and transportation of electrolyte ions; (2) the introduction of heteroatoms provides more attachment sites for electrolyte ions,[42] and the redox reaction of N/O functional groups provides additional pseudocapacitance; (3) the hierarchical pore structure formed by urea doping makes the N_ZPC_{4-700} electrodes with short and efficient electron and ion transmission pathways, thereby ensuring high capacity and rate performance.[43] Due to the increase of transmission resistance, the specific capacitance of N_3PC_{4-700} decreases with the increase of the current density (Figure 6d,e). As exhibited in Figure 6e, N_3PC_{4-700} has a capacity retention rate of 72.5% at a current density of 20 A g^{-1}, indicating its excellent rate

https://doi.org/10.1021/acsomega.2c01534
ACS Omega 2022, 7, 23342−23352

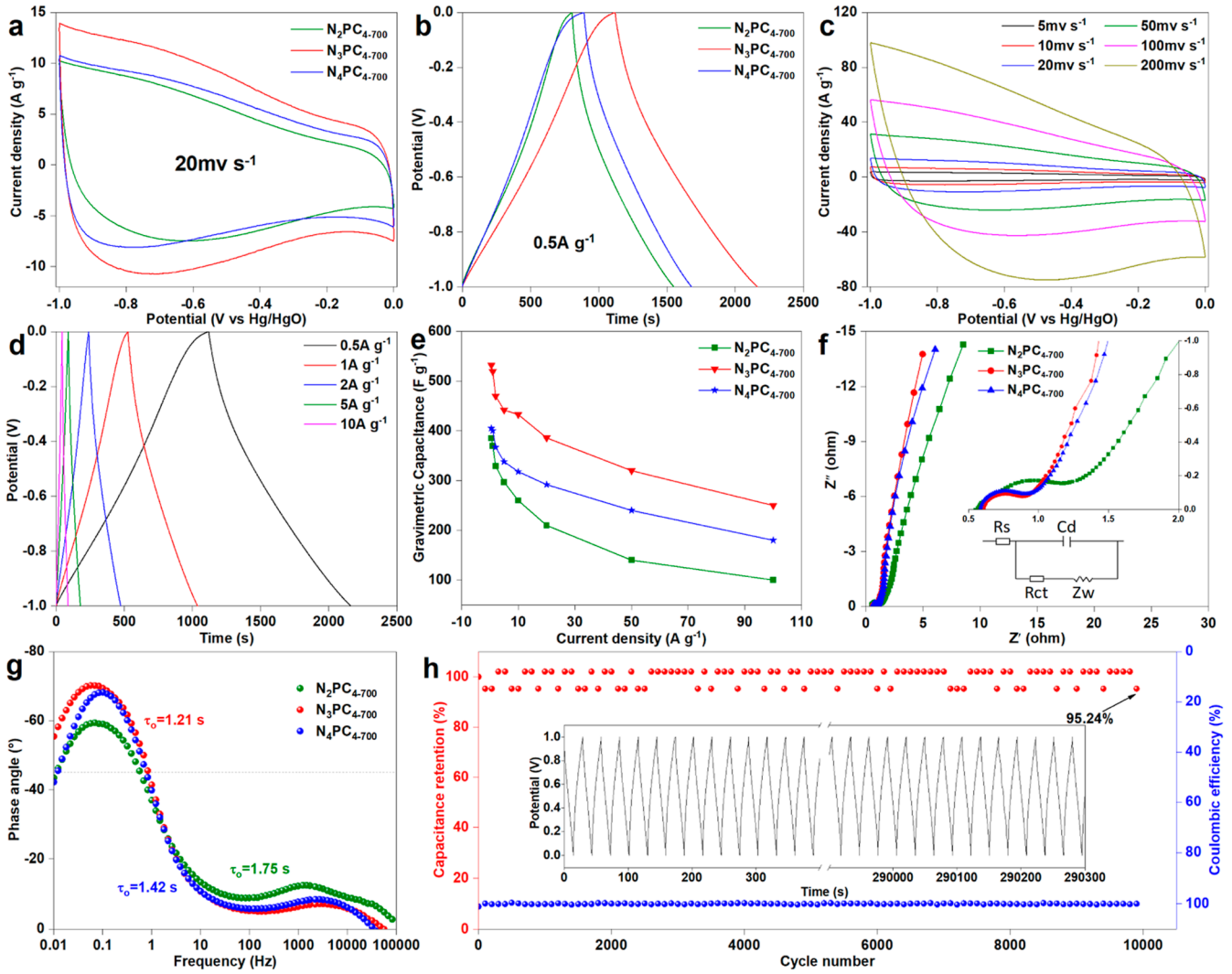

Figure 6. Electrochemical tests of $N_ZPC_{4\text{-}700}$ in a three-electrode system: (a,b) CV and GCD curves of $N_ZPC_{4\text{-}700}$, (c,d) CV and GCD curves of $N_3PC_{4\text{-}700}$, (e) corresponding rate capabilities, (f) Nyquist plots, (g) Bode plots, and (h) cycle performance and Coulombic efficiency of $N_3PC_{4\text{-}700}$ under 20 A g^{-1}.

performance. The high rate performance may be attributed to the abundant micropores for storing electrolyte ions, and N-doping improves the surface wettability of PCs and reduces the transport resistance of electrolyte ions.[44] In addition, the loading effect of active materials on the capacitance is also evident. As shown in Figure S6, the specific capacitance of $N_3PC_{4\text{-}700}$ decreases with the increase of active material loading, and its specific capacitance is 421 F g^{-1} when the mass is 5.4 mg. This is because when the mass of active materials increases, the ion migration pathway of the electrolyte becomes longer and slower, resulting in a decrease in specific capacitance.

Figure 6f shows the Nyquist plots of $N_ZPC_{4\text{-}700}$, and the equivalent circuit diagram used the nonlinear Schrodinger equation to fit the EIS data (Figure 6f inset). The intrinsic resistance (R_c) values of $N_ZPC_{4\text{-}700}$ are all less than 0.62, indicating that the internal resistance of PCs is small. In the high-frequency region, the small arc span indicates that the charge-transfer resistance (R_{ct}) value is low. $N_3PC_{4\text{-}700}$ has the lowest R_{ct} value, suggesting that its charge-transfer resistance is the lowest, which is conducive to the rapid storage and release of electrolyte ions to the electrode surface.[45] In addition, the slope of curves in the low-frequency region also has a similar trend, indicating that the mass-transfer rate between the electrode and electrolyte is accelerated. This may be due to the N-doping and layered pore structure enhancing the surface wettability and promoting the charge transfer of PCs.[46] Moreover, the relaxation time constant ($\tau_o = 1/f$, f is the frequency at −45°) obtained from the Bode plot is 1.21 s for $N_3PC_{4\text{-}700}$ (Figure 6g). The low relaxation time constant of $N_3PC_{4\text{-}700}$ means that electrolyte ions can penetrate well into the electrode material, giving it good capacitance and fast charging capabilities. Figure 6h further shows that $N_3PC_{4\text{-}700}$ has good cycle stability (95.2% capacitance retention ratio after 10,000 cycle) and a good Coulombic efficiency (100% after 10,000 cycles).

As mentioned above, $N_ZPC_{4\text{-}700}$ is dominated by electric double-layer energy storage due to its large SSA, unique hierarchical pore structure, and pseudocapacitance induced by N-doping. Therefore, the charge/discharge kinetics is qualitatively evaluated according to eqs 6 and 7[47]

$$i = a\nu^b \tag{6}$$

and

https://doi.org/10.1021/acsomega.2c01534
ACS Omega 2022, 7, 23342−23352

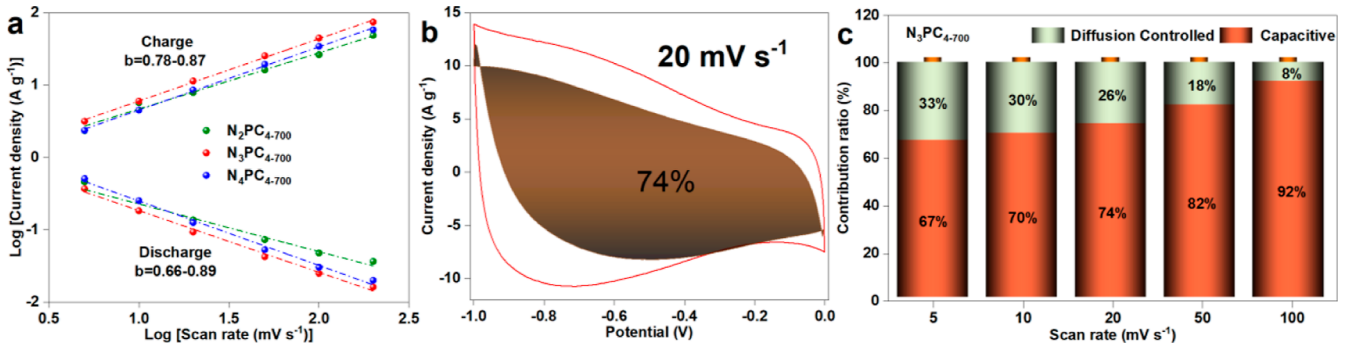

Figure 7. (a) Linear plot of log i vs log ν in both charge and discharge processes, (b) capacitive contribution at 20 mV s^{-1}, and (c) diffusion-controlled and capacitive-controlled contribution ratios at different scan rates.

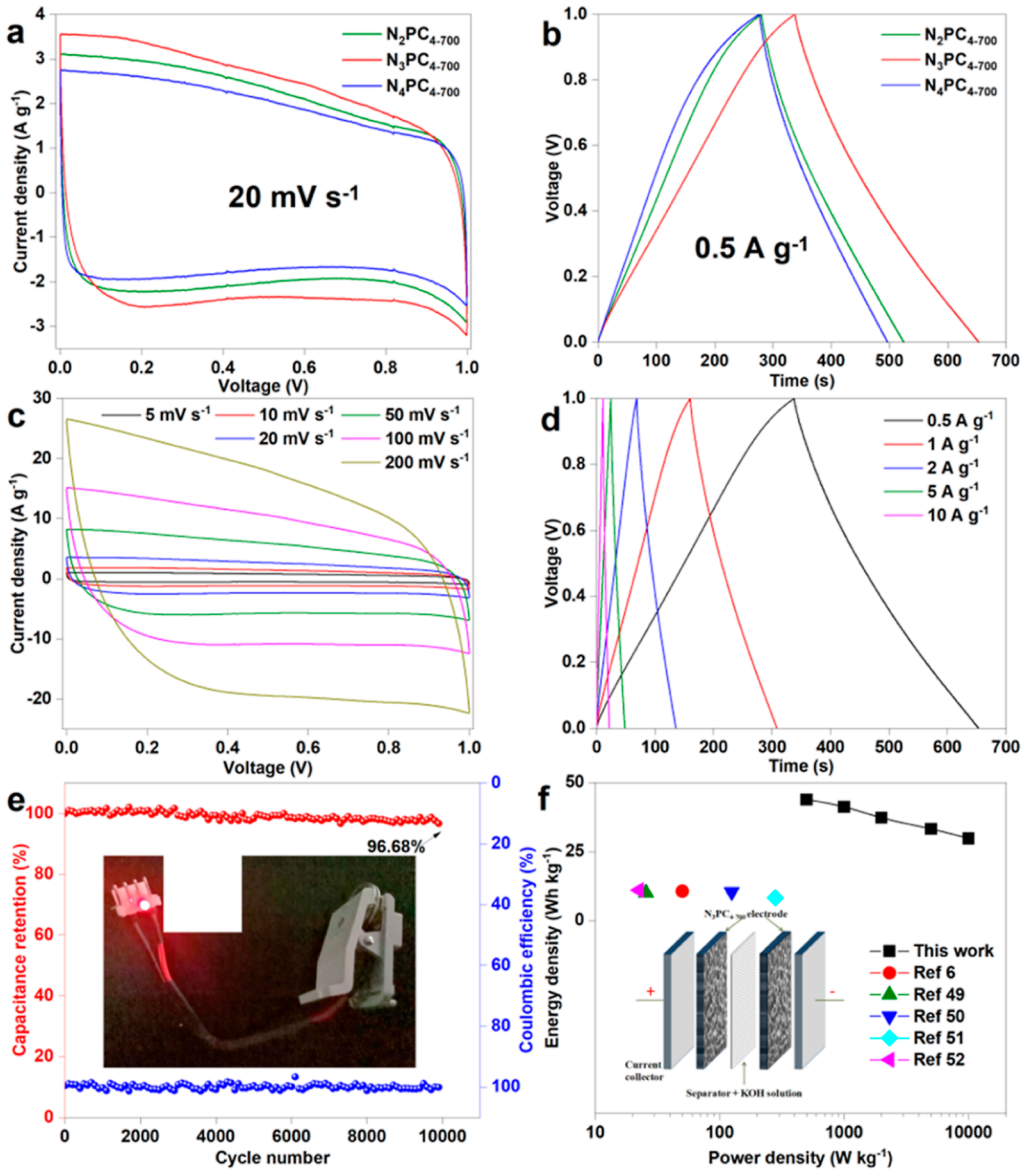

Figure 8. Electrochemical performance of a symmetric SC with a 6 M KOH electrolyte: (a,b) CV and GCD curves of $N_ZPC_{4\text{-}700}$, (c,d) CV and GCD curves of $N_3PC_{4\text{-}700}$, (e) cycle performance and Coulombic efficiency of $N_3PC_{4\text{-}700}$ under 20 A g^{-1} (inset: an LED light, powered by an assembled $N_3PC_{4\text{-}700}$-based button battery), and (f) Ragone plot.

$$\log(i) = \log(a) + b\log(\nu) \quad (7)$$

where a and b are constants, while i and v are the current density and scan rate, respectively. In general, when b is close to 0.5, the electrochemical behavior is dominated by

https://doi.org/10.1021/acsomega.2c01534
ACS Omega 2022, 7, 23342−23352

Table 2. Electrochemical Performance of the Samples

material	current density (A g^{-1})	specific capacity (F g^{-1})	energy density (Wh kg^{-1})	power density (W kg^{-1})	cycling performance (%)	reference
CTP	0.50	532.5	43.8	500.0	96.7 (10,000 cycles)	This work
CTP	0.10	320.0	10.6	50.1	94.0 (10,000 cycles)	6
CTP	1.00	228.0			94.2 (1000 cycles)	15
petroleum pitch	0.05	293.0 (2E)	10.0	25.6	97.4 (7000 cycles)	48
raw coal	0.50	298.0	10.4	125.0	95.3 (10,000 cycles)	49
graphitized coal	0.50	225.0	79.4(EMIMBF$_4$)		91.0 (10,000 cycles)	50
petroleum coke	0.05	342.8	8.2	280.0	71.8 (1000 cycles)	51
lignite[a]	0.05	390.0	11.0	22.5	94.1 (2000 cycles)	52

[a]3 M KOH, the electrolyte of other samples is 6 M KOH.

pseudocapacitance and the reaction kinetics is slow. When b is close to 1, the electrochemical behavior is dominated by electric double-layer capacitance, and the reaction kinetics is fast. As shown in Figure 7a, the calculated b values of $N_ZPC_{4\text{-}700}$ ranged from 0.66 to 0.89. Furthermore, Dunn's method was used to quantitatively analyze the capacitive contributions of the $N_ZPC_{4\text{-}700}$ surface capacitance-controlled and diffusion-controlled processes, as shown in eqs 8 and 9.[47]

$$i = k_1\nu + k_2\nu^{1/2} \tag{8}$$

and

$$i/\nu^{1/2} = k_1\nu^{1/2} + k_2 \tag{9}$$

where $k_1\nu$ and $k_2\nu^{1/2}$ represent the surface capacitance-controlled and diffusion-controlled current contributions, respectively. Figure 7b shows the surface capacitance-controlled and diffusion-controlled current contributions of $N_3PC_{4\text{-}700}$ at 20 mV s^{-1}. The results show that the surface capacitance controls the contribution of most dynamic processes. Figure 7c shows that the $N_3PC_{4\text{-}700}$ surface-controlled capacitance increases to 92% when the scan rate is as high as 100 mV s^{-1}, consistent with its high rate capability.

3.2.2. $N_ZPC_{4\text{-}700}$ Symmetric SCs. In order to further study the electrochemical performance of $N_ZPC_{4\text{-}700}$, coin-shaped symmetrical devices were assembled in 6 M KOH. As displayed in Figure 8a–d, the CV and GCD curves of $N_ZPC_{4\text{-}700}//N_ZPC_{4\text{-}700}$ symmetric SCs as well as those of $N_3PC_{4\text{-}700}//N_3PC_{4\text{-}700}$ symmetric SCs at different scan rates and current densities were tested. The specific electrochemical behavior analyses of $N_ZPC_{4\text{-}700}//N_ZPC_{4\text{-}700}$ symmetric SCs are similar to those of the three-electrode system. In addition, the specific capacitance of $N_3PC_{4\text{-}700}$ increases significantly (Figure S7), which is consistent with the analysis of the three-electrode system. As illustrated in Figure 8e, the $N_3PC_{4\text{-}700}//N_3PC_{4\text{-}700}$ symmetric SCs have good cycle stability (96.7% capacitance retention ratio after 10,000 cycle) and η (100% after 10,000 cycles). Noteworthily, the button battery with $N_3PC_{4\text{-}700}$ and zinc flakes as positive/negative materials lighted up the LED lamp, indicating that such SCs have a high practical value (Figure 8e inset). Moreover, the self-discharge performance of SCs is one of the main factors in their applications. After charging the $N_3PC_{4\text{-}700}//N_3PC_{4\text{-}700}$ symmetric SC to 1V and self-discharging for 24 h, its open-circuit voltage was 0.78 V, which maintained 78% of the initial voltage value (Figure S8).

Energy and power densities are important indicators for measuring SCs. The assembled $N_3PC_{4\text{-}700}//N_3PC_{4\text{-}700}$ symmetrical SCs can provide a maximum energy density of 43.8 W h kg^{-1} at a power density of 0.5 kW kg^{-1}. More significantly, the energy density can still be kept at 29.7 W h kg^{-1} even at a power density as high as 10 kW kg^{-1}. The electrochemical performances of some coal-based and pitch-based carbon materials are compared and listed in Table 2. The various electrochemical properties of N-doped PCs reported in this work are more prominent.

4. CONCLUSIONS

The specific capacitance of as-synthesized PCs was greatly improved under the intervention of urea. Compared with other PCs, N_3-$PC_{4\text{-}700}$ has suitable pore size distribution and a suitable N/O co-doping amount. These properties not only facilitate the penetration and absorption of electrolyte ions but also guarantee the fast and efficient electron transfer on the N_3-$PC_{4\text{-}700}$ surface. In the three-electrode system, N_3-$PC_{4\text{-}700}$ exhibits the highest specific capacitance (532.5 F g^{-1} at 0.5 A g^{-1}) and excellent rate capability (72.5% at 20 A g^{-1}). In addition, after 10,000 charge–discharge cycles, the capacitance retention and η were as high as 96.7 and 100%, respectively. In a coin-type symmetric device, the specific capacitance of N_3-$PC_{4\text{-}700}//N_3$-$PC_{4\text{-}700}$ symmetric SCs was 315.5 F g^{-1} at 0.5 A g^{-1}. The N_3-$PC_{4\text{-}700}//N_3$-$PC_{4\text{-}700}$ symmetric SCs have an energy density of 43.8 W h kg^{-1} and a power density of 0.5 kW kg^{-1} and still maintain a value of 29.7 W h kg^{-1} at 10 kW kg^{-1}. In conclusion, this work confirms that the introduction of pyridine-N and pyrrole-N can effectively improve the electrochemical performance of PCs.

■ ASSOCIATED CONTENT

Supporting Information

The Supporting Information is available free of charge at https://pubs.acs.org/doi/10.1021/acsomega.2c01534.

Nitrogen adsorption and desorption and pore size distribution diagram; SEM spectrum; XPS spectroscopy; elemental content and functional group content detected by XPS; high-resolution C 1s of the samples; and CV and GCD curves (PDF)

■ AUTHOR INFORMATION

Corresponding Authors

Cui-Ying Lu − *Shaanxi Key Laboratory of Low Metamorphic Coal Clean Utilization, School of Chemistry and Chemical Engineering, Yulin University, Yulin 719000 Shaanxi, China*; orcid.org/0000-0002-7905-2991; Phone: +86 0912 3891144; Email: lucuiying126@126.com; Fax: +86 0912 3891144

Guang-Hui Liu − *Shaanxi Key Laboratory of Low Metamorphic Coal Clean Utilization, School of Chemistry and Chemical Engineering, Yulin University, Yulin 719000*

https://doi.org/10.1021/acsomega.2c01534
ACS Omega 2022, 7, 23342−23352

Shaanxi, China; Anhui Key Laboratory of Coal Clean Conversion and High Valued Utilization, Anhui University of Technology, Ma'anshan 243002 Anhui, China; State Key Laboratory of High-efficiency Coal Utilization and Green Chemical Engineering, School of Chemistry and Chemical Engineering, Ningxia University, Yinchuan 750021 Ningxia, China; Email: tjdxlgh@163.com

Authors

Yuan-Jia Cao − *Shaanxi Key Laboratory of Low Metamorphic Coal Clean Utilization, School of Chemistry and Chemical Engineering, Yulin University, Yulin 719000 Shaanxi, China*

Zhi-Wen Zhang − *Shaanxi Key Laboratory of Low Metamorphic Coal Clean Utilization, School of Chemistry and Chemical Engineering, Yulin University, Yulin 719000 Shaanxi, China*

Zhen Wang − *Shaanxi Key Laboratory of Low Metamorphic Coal Clean Utilization, School of Chemistry and Chemical Engineering, Yulin University, Yulin 719000 Shaanxi, China*

Yu-Hong Kang − *Shaanxi Key Laboratory of Low Metamorphic Coal Clean Utilization, School of Chemistry and Chemical Engineering, Yulin University, Yulin 719000 Shaanxi, China*

Ting-Ting Yang − *Shaanxi Key Laboratory of Low Metamorphic Coal Clean Utilization, School of Chemistry and Chemical Engineering, Yulin University, Yulin 719000 Shaanxi, China*

Xian-Yong Wei − *Shaanxi Key Laboratory of Low Metamorphic Coal Clean Utilization, School of Chemistry and Chemical Engineering, Yulin University, Yulin 719000 Shaanxi, China; State Key Laboratory of High-efficiency Coal Utilization and Green Chemical Engineering, School of Chemistry and Chemical Engineering, Ningxia University, Yinchuan 750021 Ningxia, China; Key Laboratory of Coal Processing and Efficient Utilization, Ministry of Education, China University of Mining & Technology, Xuzhou 221116 Jiangsu, China*; orcid.org/0000-0001-7106-4624

Hong-Cun Bai − *State Key Laboratory of High-efficiency Coal Utilization and Green Chemical Engineering, School of Chemistry and Chemical Engineering, Ningxia University, Yinchuan 750021 Ningxia, China*

Complete contact information is available at: https://pubs.acs.org/10.1021/acsomega.2c01534

Notes

The authors declare no competing financial interest.

■ ACKNOWLEDGMENTS

This work was supported by the National Natural Science Foundation of China (Grants 22108237 and 22068038), the Natural Science Foundation Research Program of Shaanxi province (Grant 2021JQ-830), the Natural Special Project of Shaanxi Provincial Department of Education (Grant 21JK1011), the Foundation of State Key Laboratory of High-efficiency Utilization of Coal and Green Chemical Engineering (Grant 2021-K74), the Anhui Province Key Laboratory of Coal Clean Conversion and High Valued Utilization, Anhui University of Technology (Grant CHV21-01), the Yulin Science and Technology Plan Project (Grants CXY-2021-105−02 and 2019-82-2), the Industry University Research Cooperation Project of Yulin High-tech Zone (Grants CXY-2020-01 and CXY-2021-23), the Joint Fund Project of Yulin University-Dalian National Laboratory for Clean Energy (Grant YLU-DNL Fund 2021009), the Shaanxi Province Science and Technology Resources Open Sharing Platform Project (Grant 2019PT-18), and the Initial Scientific Research Fund of High Level Talents in Yulin university (Grant 21GK03).

■ NOMENCLATURE

BET	Brunauer−Emmett−Teller
C	capacitance
CTP	coal tar pitch
CV	cyclic voltammetry
DFT	density functional theory
EIS	electrochemical impedance spectroscopy
GCD	galvanostatic charge−discharge
N_1	pyridine-N
N_2	pyrrole-N
N_3	graphite-N
N_4	N-oxides
PC	porous carbon
PTFE	polytetrafluoroethylene
PV	pore volume
R_c	intrinsic resistance
R_{ct}	charge-transfer resistance
SC	supercapacitor
SEM	scanning electron microscopy
SSA	specific surface area
TEM	transmission electron microscopy
XPS	X-ray photoelectron spectroscopy
XRD	X-ray diffraction
η	Coulombic efficiency

■ REFERENCES

(1) Wu, X.; Han, Z.; Zheng, X.; Yao, S.; Yang, X.; Zhai, T. Core-shell structured Co_3O_4@ $NiCo_2O_4$ electrodes grown on fexible carbon fbers with superior electrochemical properties. *Nano Energy* **2017**, *31*, 410−417.

(2) Sevilla, M.; Fuertes, A. B. Direct synthesis of highly porous interconnected carbon nanosheets and their application as high-performance supercapacitors. *ACS Nano* **2014**, *8*, 5069−5078.

(3) Li, S. High−performance Activated Carbons Prepared by KOH Activation of Gulfweed for supercapacitors. *Int. J. Electrochem. Sci.* **2018**, *13*, 1728−1743.

(4) Miao, L.; Duan, H.; Liu, M.; Lu, W.; Zhu, D.; Chen, T.; Li, L.; Gan, L. Poly(ionic liquid)-derived, N, S-codoped ultramicroporous carbon nanoparticles for supercapacitors. *Chem. Eng. J.* **2017**, *317*, 651−659.

(5) Jiang, M.; Sun, N.; Ali Soomro, R.; Xu, B. The recent progress of pitch-based carbon anodes in sodium-ion batteries. *J. Energy Chem.* **2021**, *55*, 34−47.

(6) Liu, H.; Song, H.; Hou, W.; Chang, Y.; Zhang, Y.; Li, Y.; Zhao, Y.; Han, G. Coal tar pitch-based hierarchical porous carbons prepared in molten salt for supercapacitors. *Mater. Chem. Phys.* **2021**, *265*, 124491.

(7) Lee, M. S.; Choi, H.-J.; Baek, J.-B.; Chang, D. W. Simple solution-based synthesis of pyridinic-rich nitrogen-doped graphene nanoplatelets for supercapacitors. *Appl. Energy* **2017**, *195*, 1071−1078.

(8) Xu, R.-X.; Zhao, Y.-P.; Liu, G.-H.; Zhu, J.-S.; Wang, R.-Y.; Cao, J.-P.; Wei, X.-Y. N/O co-doped porous interconnected carbon nanosheets from the co-hydrothermal treatment of soybean stalk and nickel nitrate for high-performance supercapacitors. *J. Colloid Interface Sci.* **2020**, *558*, 211−219.

(9) Ding, Y.; Mo, L. e.; Gao, C.; Liu, X.; Yu, T.; Chen, W.; Chen, S.; Li, Z.; Hu, L. High-Surface-Area Porous Carbon Flakes Derived from Boat-Fruited Sterculia Seeds for High-Energy-Density Aqueous

Symmetric supercapacitors. *ACS Sustainable Chem. Eng.* **2018**, *6*, 9822−9830.
(10) Deng, Y.; Xie, Y.; Zou, K.; Ji, X. Review on recent advances in nitrogen-doped carbons: preparations and applications in supercapacitors. *J.Mater.Chem.A* **2016**, *4*, 1144−1173.
(11) Chen, J.; Xu, J.; Zhou, S.; Zhao, N.; Wong, C.-P. Nitrogen-doped hierarchically porous carbon foam: a free-standing electrode and mechanical support for high-performance supercapacitors. *Nano Energy* **2016**, *25*, 193−202.
(12) Ghosh, S.; Barg, S.; Jeong, S. M.; Ostrikov, K. Heteroatom-Doped and Oxygen-Functionalized Nanocarbons for High-Performance Supercapacitors. *Adv. Energy Mater.* **2020**, *10*, 2001239.
(13) Wan, L.; Wang, J.; Xie, L.; Sun, Y.; Li, K. Nitrogen-Enriched Hierarchically Porous Carbons Prepared from Polybenzoxazine for High-Performance supercapacitors. *ACS Appl. Mater. Inter.* **2014**, *6*, 15583−15596.
(14) Wang, F. P.; Zheng, F. H.; Jiang, J. T.; Li, Y. H.; Luo, Y. T.; Chen, K. B.; DuHuang, J. Y. G.; Li, Q. Y.; Wang, H. Q. Microwave-Assisted Preparation of Hierarchical N and O Co-Doped Corn-Cob-Derived Activated Carbon for a High-Performance SCs. *Energy Fuels* **2021**, *35*, 8334−8344.
(15) Zhong, C.; Gong, S.; Jin, L. E.; Li, P.; Cao, Q. Preparation of nitrogen-doped pitch-based carbon materials for supercapacitors. *Mater. Lett.* **2015**, *156*, 1−6.
(16) Zhao, Y. P.; Xu, R. X.; Cao, J. P.; Zhang, X. Y.; Zhu, J. S.; Wei, X. Y. N/O co-doped interlinked porous carbon nanoflakes derived from soybean stalk for high-performance supercapacitors. *J. Electroanal. Chem.* **2020**, *871*, 114288−114296.
(17) Zhang, G.; Sun, Y.; Xu, Y.; Zhang, R. Catalytic performance of N-doped activated carbon supported cobalt catalyst for carbon dioxide reforming of methane to synthesis gas. *J. Taiwan Inst. Chem. Eng.* **2018**, *93*, 234−244.
(18) Lei, S.; Chen, L.; Zhou, W.; Deng, P.; Liu, Y.; Fei, L.; Lu, W.; Xiao, Y.; Cheng, B. Tetra-heteroatom self-doped carbon nanosheets derived from silkworm excrement for high-performance supercapacitors. *J. Power Sources* **2018**, *379*, 74−83.
(19) Wei, W.; Chen, Z.; Zhang, Y.; Chen, J.; Wan, L.; Du, C.; Xie, M.; Guo, X. Full-faradaic-active nitrogen species doping enables high-energy-density carbon-based supercapacitor. *J. Energy Chem.* **2020**, *48*, 277−284.
(20) Yin, F.; Lu, K.-L.; Wei, X.-Y.; Fan, Z.-C.; Li, J.-H.; Kong, Q.-Q.; Zong, Z.-M.; Bai, H.-C. Fabrication of N/O self-doped hierarchical porous carbons derived from modified coal tar pitch for high-performance supercapacitors. *Fuel* **2022**, *310*, 122418.
(21) Gao, Y.; Yue, Q.; Gao, B.; Li, A. Insight into activated carbon from different kinds of chemical activating agents: A review. *Sci. Total Environ.* **2020**, *746*, 141094−141112.
(22) Xie, M.; Meng, H.; Chen, J.; Zhang, Y.; Du, C.; Wan, L.; Chen, Y. High-Volumetric Supercapacitor Performance of Ordered Mesoporous Carbon Electrodes Enabled by the Faradaic-Active Nitrogen Doping and Decrease of Microporosity. *ACS Appl. Energy Mater.* **2021**, *4*, 1840−1850.
(23) Wang, Q.; Liu, F.; Jin, Z.; Qiao, X.; Huang, H.; Chu, X.; Xiong, D.; Zhang, H.; Liu, Y.; Yang, W. Hierarchically Divacancy Defect Building Dual-Activated Porous Carbon Fibers for High-Performance Energy-Storage Devices. *Adv. Funct. Mater.* **2020**, *30*, 2002580.
(24) Wang, Q.; Zhou, Y.; Zhao, X.; Chen, K.; Bingni, G.; Yang, T.; Zhang, H.; Yang, W.; Chen, J. Tailoring carbon nanomaterials via a molecular scissor. *Nano Today* **2021**, *36*, 101033.
(25) Chen, K.; Shi, B.; Yue, Y.; Qi, J.; Guo, L. Binary synergy strengthening and toughening of bio-inspired nacre-like graphene oxide/sodium alginate composite paper. *ACS Nano* **2015**, *9*, 8165−8175.
(26) Hu, X.; Rajendran, S.; Yao, Y.; Liu, Z.; Gopalsamy, K.; Peng, L.; Gao, C. A novel wet-spinning method of manufacturing continuous bio-inspired composites based on graphene oxide and sodium alginate. *Nano Res.* **2016**, *9*, 735−744.
(27) Wang, Q.; Chen, Y.; Jiang, X.; Qiao, X.; Wang, Y.; Zhao, H.; Pu, B.; Yang, W. Self-assembly defect-regulating superstructured carbon. *Energy Storage Mater.* **2022**, *48*, 164−171.
(28) Liu, F.; Wang, Z.; Zhang, H.; Jin, L.; Chu, X.; Gu, B.; Huang, H.; Yang, W. Nitrogen, oxygen and sulfur co-doped hierarchical porous carbons toward high-performance supercapacitors by direct pyrolysis of kraft lignin. *Carbon* **2019**, *149*, 105−116.
(29) Yoshikawa, Y.; Teshima, K.; Futamura, R.; Tanaka, H.; Neimark, A. V.; Kaneko, K. Structural mechanism of reactivation with steam of pitch-based activated carbon fibers. *J. Colloid Interface Sci.* **2020**, *578*, 422−430.
(30) Bo, X.; Xiang, K.; Zhang, Y.; Shen, Y.; Chen, S.; Wang, Y.; Xie, M.; Guo, X. Microwave-assisted conversion of biomass wastes to pseudocapacitive mesoporous carbon for high-performance supercapacitor. *J. Energy Chem.* **2019**, *39*, 1−7.
(31) Liang, J.; Qu, T.; Kun, X.; Zhang, Y.; Chen, S.; Cao, Y.-C.; Xie, M.; Guo, X. Microwave assisted synthesis of camellia oleifera shell-derived porous carbon with rich oxygen functionalities and superior supercapacitor performance. *Appl. Surf. Sci.* **2018**, *436*, 934−940.
(32) Naushad, M.; Ahamad, T.; Al-Maswari, B. M.; Abdullah Alqadami, A.; Alshehri, S. M. Nickel ferrite bearing nitrogen-doped mesoporous carbon as efficient adsorbent for the removal of highly toxic metal ion from aqueous medium. *Chem. Eng. J.* **2017**, *330*, 1351−1360.
(33) Guan, L.; Pan, L.; Peng, T.; Gao, C.; Zhao, W.; Yang, Z.; Hu, H.; Wu, M. Synthesis of biomass-derived nitrogen-doped porous carbon nanosheests for high-performance supercapacitors. *ACS Sustainable Chem. Eng.* **2019**, *7*, 8405−8412.
(34) Phiri, J.; Dou, J.; Vuorinen, T.; Gane, P. A. C.; Maloney, T. C. Highly porous willow wood-derived activated carbon for high-performance SCs electrodes. *ACS Omega* **2019**, *4*, 18108−18117.
(35) Luo, W.; Wang, B.; Heron, C. G.; Allen, M. J.; Morre, J.; Maier, C. S.; Stickle, W. F.; Ji, X. Pyrolysis of Cellulose under Ammonia Leads to Nitrogen-Doped Nanoporous Carbon Generated through Methane Formation. *Nano Lett.* **2014**, *14*, 2225−2229.
(36) Li, B.; Dai, F.; Xiao, Q.; Yang, L.; Shen, J.; Zhang, C.; Cai, M. Nitrogen-doped activated carbon for high energy hybrid SCs. *Energy Environ. Sci.* **2016**, *9*, 102−106.
(37) Fu, G.; Li, Q.; Ye, J.; Han, J.; Wang, J.; Zhai, L.; Zhu, Y. Hierarchical porous carbon with high nitrogen content derived from plant waste (pomelo peel) for SCs. *J. Mater. Sci.* **2018**, *29*, 7707−7717.
(38) Zhao, Y.-Q.; Lu, M.; Tao, P.-Y.; Zhang, Y.-J.; Gong, X.-T.; Yang, Z.; Zhang, G.-Q.; Li, H.-L. Hierarchically porous and heteroatom doped carbon derived from tobacco rods for supercapacitors. *J. Power Sources* **2016**, *307*, 391−400.
(39) Wang, Y.; Xia, Y. Recent Progress in supercapacitors: From Materials Design to System Construction. *Adv. Mater.* **2013**, *25*, 5336−5342.
(40) Liu, H.; Song, H.; Chen, X.; Zhang, S.; Zhou, J.; Ma, Z. Effects of nitrogen- and oxygen-containing functional groups of activated carbon nanotubes on the electrochemical performance in supercapacitors. *J. Power Sources* **2015**, *285*, 303−309.
(41) Zhang, S.; Yu, Y.; Xie, M.; Du, C.; Chen, J.; Wan, L.; Zhang, Y. Clean production of N, O-doped activated carbon by water vapor carbonization/activation of expired coffee for high-volumetric supercapacitor. *Appl. Surf. Sci.* **2022**, *589*, 153011.
(42) Zhao, H.; Xing, B.; Zhang, C.; Huang, G.; Liu, Q.; Yi, G.; Jia, J.; Ma, M.; Chen, Z.; Zhang, C. Efficient synthesis of nitrogen and oxygen co-doped hierarchical porous carbons derived from soybean meal for high-performance supercapacitors. *J. Alloys Compd.* **2018**, *766*, 705−715.
(43) Yue, Y.; Liang, H. Hierarchical micro-architectures of electrodes for energy storage. *J. Power Sources* **2015**, *284*, 435−445.
(44) Peng, H.; Ma, G.; Sun, K.; Zhang, Z.; Yang, Q.; Lei, Z. Nitrogen-doped interconnected carbon nanosheets from pomelo mesocarps for high performance supercapacitors. *Electrochim. Acta* **2016**, *190*, 862−871.

https://doi.org/10.1021/acsomega.2c01534
ACS Omega 2022, 7, 23342−23352

(45) Wang, H.; Li, Z.; Tak, J. K.; Holt, C. M. B.; Tan, X.; Xu, Z.; Amirkhiz, B. S.; Harfield, D.; Anyia, A.; Stephenson, T.; Mitlin, D. supercapacitors based on carbons with tuned porosity derived from paper pulp mill sludge biowaste. *Carbon* **2013**, *57*, 317−328.
(46) Li, Y.; Wang, G.; Wei, T.; Fan, Z.; Yan, P. Nitrogen and sulfur co-doped porous carbon nanosheets derived from willow catkin for supercapacitors. *Nano Energy* **2016**, *19*, 165−175.
(47) Yang, X.; Zhao, S.; Zhang, Z.; Chi, Y.; Yang, C.; Wang, C.; Zhen, Y.; Wang, D.; Fu, F.; Chi, R. A. Pore structure regulation of hierarchical porous carbon derived from coal tar pitch via pre-oxidation strategy for high-performance supercapacitor. *J. Colloid Interface Sci.* **2022**, *614*, 298−309.
(48) Liu, M.-j.; Wei, F.; Yang, X.-m.; Dong, S.-a.; Li, Y.-j.; He, X.-j. Synthesis of porous graphene-like carbon materials for high-performance supercapacitors from petroleum pitch using nano-$CaCO_3$ as a template. *New Res. Carbon Mater.* **2018**, *33*, 316−323.
(49) Dong, D.; Zhang, Y.; Xiao, Y.; Wang, T.; Wang, J.; Gao, W. Oxygen-enriched coal-based porous carbon under plasma-assisted $MgCO_3$ activation as SCs electrodes. *Fuel* **2022**, *309*, 122168−122177.
(50) Sun, L.; Zhao, Z.; Sun, Y.; Wang, X.; Liu, X.; Yang, Y.; Qiu, J. Activated coal-based graphene with hierarchical porous structures for ultrahigh energy density supercapacitors. *Diamond Relat. Mater.* **2020**, *106*, 107827−107834.
(51) He, X.; Geng, Y.; Qiu, J.; Zheng, M.; Zhang, X.; Shui, H. Influence of KOH/Coke Mass Ratio on Properties of Activated Carbons Made by Microwave-Assisted Activation for Electric DoubleLayer Capacitors. *Energy Fuels* **2010**, *24*, 3603−3609.
(52) Xing, B.; Huang, G.; Chen, L.; Guo, H.; Zhang, C.; Xie, W.; Chen, Z. Microwave Synthesis of Hierarchically Porous Activated Carbon from Lignite for High Performance supercapacitors. *J. Porous Mater.* **2016**, *23*, 67−73.

https://doi.org/10.1021/acsomega.2c01534
ACS Omega 2022, 7, 23342−23352